



## Article

# Management of $\gamma$ -Alumina with High-Efficient {111} External Surfaces for HDS Reactions

Yingrui Xu <sup>1</sup>, Shunqin Liang <sup>2</sup>, Limin Sun <sup>2</sup>, Xiaoli Hu <sup>2</sup>, Yuqi Zhang <sup>1</sup>, Weikun Lai <sup>1</sup> ,  
Xiaodong Yi <sup>1,\*</sup>  and Weiping Fang <sup>1,\*</sup>

<sup>1</sup> National Engineering Laboratory for Green Chemical Productions of Alcohols-Ethers-Esters, College of Chemistry and Chemical Engineering, Xiamen University, Xiamen 361005, China; 20520150150314@stu.xmu.edu.cn (Y.X.); 20520171151373@stu.xmu.edu.cn (Y.Z.); laiweikun@xmu.edu.cn (W.L.)

<sup>2</sup> PetroChina Lanzhou Petrochemical Research Center, Lanzhou 730000, China; liangshunqin@petrochina.com.cn (S.L.); sunlimin1@petrochina.com.cn (L.S.); huxiaoli6@petrochina.com.cn (X.H.)

\* Correspondence: xdyi@xmu.edu.cn (X.Y.); wpfang@xmu.edu.cn (W.F.)

Received: 17 September 2020; Accepted: 22 October 2020; Published: 30 October 2020



**Abstract:** A series of  $\gamma$ -alumina samples with different exposure ratio of {111} facet were synthesized by an efficient hydrothermal method via adjusting the pH value of the gel precursor. The nanorod alumina supported catalyst with the highest exposure of {111} facet exhibited the best hydrodesulfurization (HDS) activities of both thiophene and dibenzothiophene (DBT). Characterization of the sulfided NiMo/Al<sub>2</sub>O<sub>3</sub> catalyst with preferential exposure of {111} facet showed that the MoS<sub>2</sub> nano slabs were inclined to distribute in the direction along the edges of alumina nanocrystal in reduced stacking layers. The selective exposure of {111} facet played a decisive role in obtaining alumina-supported HDS catalysts with improved intrinsic activity. This work helps to better understand the relationship between catalytic properties and varied support surfaces, which demonstrate a proper design of the catalyst support morphology on the facet-level.

**Keywords:** Thiophene hydrodesulfurization; dibenzothiophene; alumina nanorods; {111} facet

## 1. Introduction

Recently, with increasing concern for environmental issues, high-quality ultra-clean fuel production from heavy crude oils has been required to have more rigid regulations and has drawn more attention in this domain. Among various proposed techniques for removing the sulfur contaminants, catalytic hydrotreating is the most widely used method in the industry. Numerous studies in the field of catalytic hydrotreating, including hydrodesulfurization (HDS), have been launched over the past decades, mainly concentrating on the development of catalysts. Traditional HDS catalysts consist mainly of active components MoS<sub>2</sub> or WS<sub>2</sub> promoted with Ni or Co loading on oxide support with high surface area [1–3].

The catalyst support plays an important role in the distribution active phase and determining catalytic performance. For the HDS catalyst, the most frequently used support is alumina [4–8] owing to its tunable and stable mechanical characteristics and low cost, yet conventional alumina interacts strongly with metal oxide precursors, which may affect their sulfidity [9]. Until recently, the exact role of how oxide affects the activities of catalysts is still not entirely resolved [10]. Based on progress in crystallization and characterization, faceted oxides crystals such as ZrO<sub>2</sub> and TiO<sub>2</sub> were carefully prepared and investigated as catalysts or supports. Support was reported controlling the orientation, growth, and shape of sulfides through a strong chemical bonding or interaction between

MoS<sub>2</sub> clusters and the oxide support along the specific facet of supports [9,11]. Elongated MoS<sub>2</sub> slabs are located parallelly or perpendicularly to the [001] and [110] direction due to the formation of Mo-S(O)-Ti linkage on the TiO<sub>2</sub> surface [12,13], while MoS<sub>2</sub> slabs lie flatly on the planar rutile TiO<sub>2</sub> (110) surface [14]. Besides, the ZnO (001) facet and (100) facet is also related to the polarity of supports and corresponding catalysts presented desulfurization activity [15], which corroborated previous studies on the TiO<sub>2</sub> that increasing (001) facet ratio led to an increase in the adsorption and catalytic properties [16]. Sulfided Co<sub>3</sub>O<sub>4</sub> nanorods with a preferred growth direction along (110) exhibit much higher HDS activity than nanopolyhedra enclosed by the (111) and (100) facets [17]. Above all, these results demonstrated that the different exposed facets of support should be involved to explain the distinct performance.

The MoS<sub>2</sub> slabs growth on conventional alumina has also been debated for decades and remains an open question due to the alumina structure and poor contrast in TEM [18,19]. The discussions about the properties of  $\gamma$ -Al<sub>2</sub>O<sub>3</sub> surfaces on a molecular level have been launched through both Density Functional Theory (DFT) modeling [10,12,20] and experimental method [10,21]. It was difficult to discriminate against the MoS<sub>2</sub> growth orientation and Al<sub>2</sub>O<sub>3</sub> basal and edge-bonded MoS<sub>2</sub> in the porous Al<sub>2</sub>O<sub>3</sub> [22]. Hence, the  $\gamma$ -Al<sub>2</sub>O<sub>3</sub> films with (100), (110), and (111) plane [23,24] and well-defined surfaces of  $\alpha$ -Al<sub>2</sub>O<sub>3</sub> [25] with different facets were synthesized. It was found that the facets of Al<sub>2</sub>O<sub>3</sub> crystal not only determined the morphology, sulfidation rate, orientation, and reactivity of MoS<sub>2</sub> nanoparticles, but also affected the surface acid/base properties [26]. Compared with  $\alpha$  polymorphs,  $\gamma$ -Al<sub>2</sub>O<sub>3</sub> is less straightforward and possess different surface OH speciation and surface properties [20]. Therefore, more work toward the effect of conventional  $\gamma$ -Al<sub>2</sub>O<sub>3</sub> facets on the interfacial Mo atoms and the Mo-O-Al linkages is needed.

In this work, we aim to understand the relationship between alumina facets and catalytic HDS performance over the NiMo/ $\gamma$ -Al<sub>2</sub>O<sub>3</sub> catalyst. A series of  $\gamma$ -Al<sub>2</sub>O<sub>3</sub> nanoparticles with various morphologies and different exposure ratios of {111} facet was synthesized by the hydrothermal method via adjusting the pH of the gel. After the loading of the Ni and Mo components, their catalytic activities were evaluated in HDS of thiophene and dibenzothiophene (DBT). The results show that the exposed facet of alumina has an important influence on the HDS activities of NiMo/Al<sub>2</sub>O<sub>3</sub> catalyst.

## 2. Results and Discussion

### 2.1. Preparation of the Alumina with Varied {111} Facet Ratios

The alumina samples were prepared by the hydrothermal process except for commercial support. As shown in Figure 1, three pH values (pH = ca. 5, 7, 10) were selected for alumina preparation as the synthesis pH is a predominant factor in determining the ultimate morphology of the resulting nanocrystals. When the gel was used as the seal for hydrothermal treatment without tuning the pH by acetic acid or NH<sub>3</sub>, rod-like alumina formed under pH = 5 with an average length of 150 nm and a width of 15 nm (Figure 1c,d). After calcination, mesopores emerged as dehydration occurred between the layered structure of  $\gamma$ -AlOOH [27]. When the synthesis pH was tuned to 7 by ammonia, the nanocrystals tended to become hexagonal prisms (donated as AH) with a smaller length to width values, indicating a relatively high sensitivity of the relative growth rates of different faces in this pH regime. As the pH was tuned to over 10, the rhombohedral nanoparticles emerge (labeled as AR), which were the most commonly viewed shape for conventional alumina and boehmite particles [20].

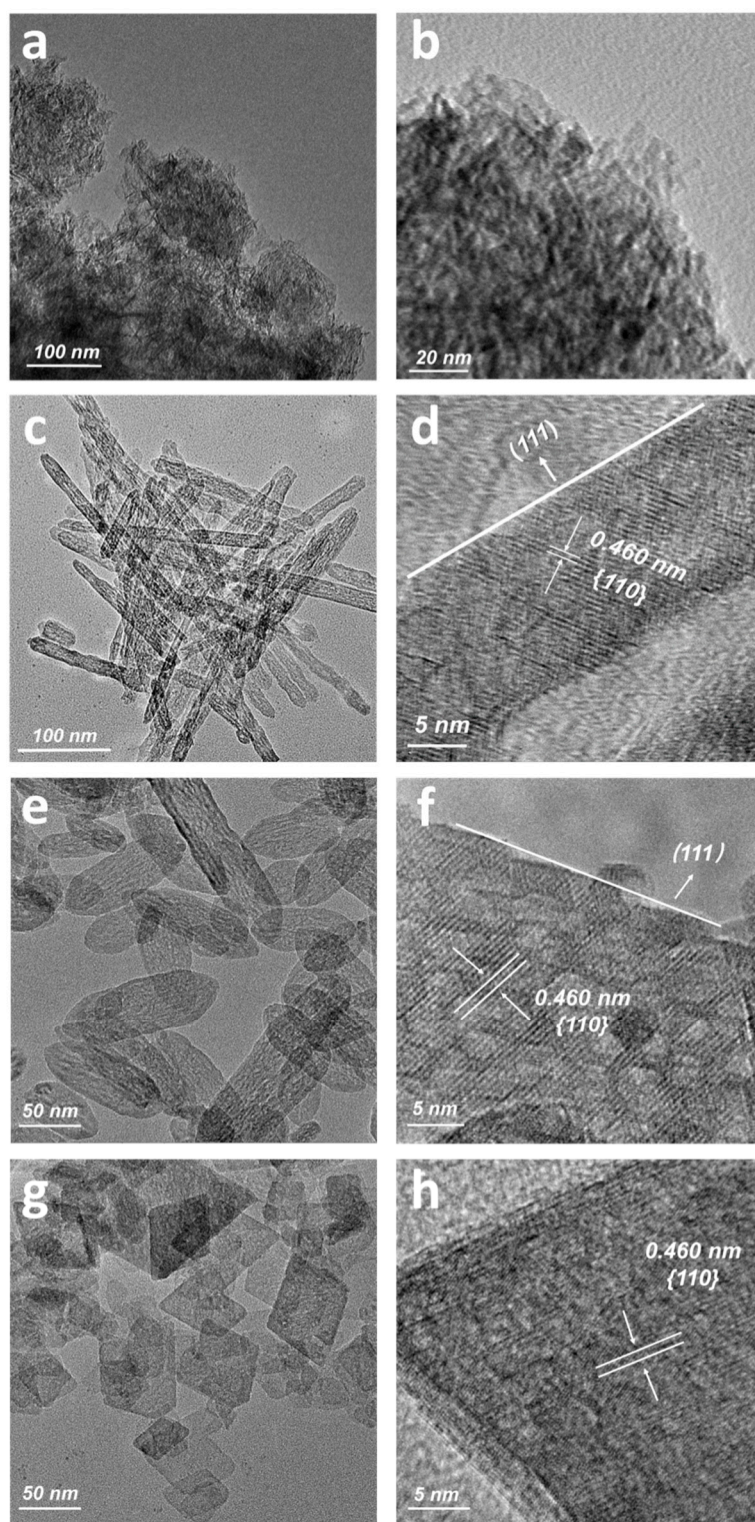


**Figure 1.** TEM images of the  $\gamma$ -alumina samples (a,b) CA; (c,d) AN; (e,f) AH; (g,h) AR.

In High Resolution Transmission Electron Microscope (HRTEM) images, the rod-like morphology was similar to the previously reported nano-tubular structure with high-energy  $\{111\}$  facet as the main external surface [28], while the corresponding lattice fringes of planes exhibited a d-spacing of 0.460 nm (Figure 1). The alumina prepared with initial gel tuned at pH = 7 and 13 were hexagonal (Figure 1e,f) and rhombohedral (Figure 1g,h) platelets, respectively. The essential parameters for the calculation of the facet ratio by HRTEM measurements were indexed in Scheme S1, where the two

nanoplates prepared under pH at 7 and 13 could be regarded as nanorods with smaller length to width ( $l/w$ ) ratios. The average  $l/w$  ratio decreased with the elevation of pH, which was consistent with the previous study [29]. In this research, only the {111} facet was calculated. The results showed that the aspect of high-energy surface {111} decreased with increased pH (Table 1). In contrast, the commercial alumina was observed to be consisting of irregular spheres with no obvious lattice fringes detectable. (Figure 1a,b) The diffraction patterns of the three as prepared alumina samples exposed higher diffraction intensity than the commercial sample, indicating higher crystallinity under the aforementioned synthesis conditions. For the commercial alumina, the (110) facet was considered to be the predominant surface [20]. This is because the domination of (010) facet on  $\text{AlOOH}$  owing to its lowest interfacial tension independent of the pH, and the (010) facet on  $\text{AlOOH}$  correspondence with (111) facet on  $\gamma\text{-Al}_2\text{O}_3$  in the topology [30].

**Table 1.** Texture properties and (111) facet portions of the alumina samples.

Samples	Targeted pH	$p^a$	Surface Area ( $\text{m}^2 \text{g}^{-1}$ )	Pore Volume ( $\text{cm}^3 \text{g}^{-1}$ )	Pore Size (nm)	$S_{(111)}^d$
AN	5	0.4 <sup>b</sup>	110.7	0.42	15.0	44.3
CA	11	0.1 <sup>c</sup>	254.8	0.68	7.5	25.4
AH	10	0.1 <sup>b</sup>	115.4	0.33	11.9	11.5
AR	13	0 <sup>b</sup>	147.4	0.55	13.5	0

<sup>a</sup>  $p$  is defined as the value of (111) facet proportion. <sup>b</sup> Experimental value. <sup>c</sup> Theoretical values [20]. <sup>d</sup>  $S_{(111)}$  is defined as the  $S_{(111)} = (\text{111) facet proportion} \times \text{surface area}$ .

As is shown in Figure 2, the as-prepared alumina samples are all posing similar diffraction peaks in XRD patterns, indicate highly crystalline and well-defined nanocrystals. The diffraction peaks at  $19.8^\circ$ ,  $31.9^\circ$ ,  $37.4^\circ$ ,  $39.7^\circ$ ,  $46.8^\circ$ , and  $66.9^\circ$  can be indexed to typical  $\gamma\text{-Al}_2\text{O}_3$ , which are in good agreement with reference data (JCPDS 00-004-0875), while no peaks from other phases were observed, indicating the high purity of the products. The diffraction patterns of the three as prepared alumina samples exposed higher diffraction intensity than the commercial sample, indicating higher crystallinity under the aforementioned synthesis conditions.

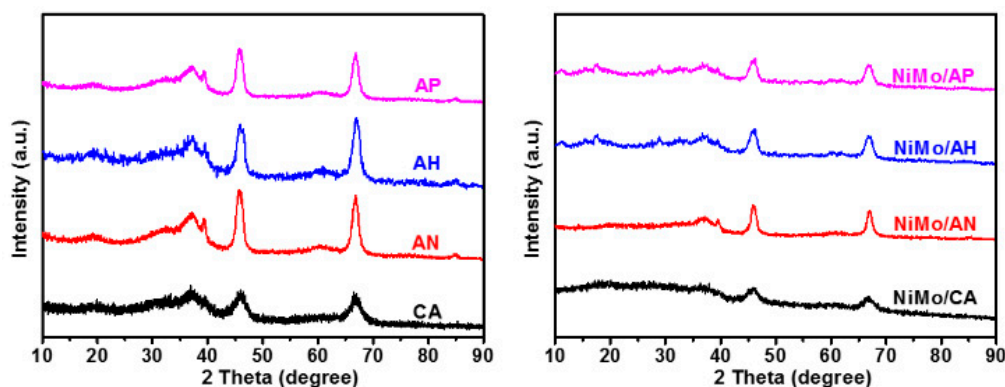


**Figure 2.** XRD of the  $\text{Al}_2\text{O}_3$  (left) and  $\text{NiMo}/\text{Al}_2\text{O}_3$  (right) samples.

## 2.2. Physiochemical Properties

The surface area and porosities of the alumina samples were investigated by  $\text{N}_2$  adsorption–desorption analysis and detailed texture parameters, including the surface areas from Brunauer–Emmett–Teller (BET) analysis and the pore volumes from the Barrett–Joyner–Halenda (BJH) method are shown in Figure S1 and Table 1. It can be noted that the commercial alumina exposed a rather large surface area ( $254.8 \text{ m}^2 \text{g}^{-1}$ ). In contrast, the as-synthesized alumina exhibit relatively low surface areas ( $110.7$ ,  $115.4$ , and  $147.4 \text{ m}^2 \text{g}^{-1}$ , respectively). The pore volume of commercial alumina is pretty large ( $0.68 \text{ cm}^3 \text{g}^{-1}$ ) compared to the samples prepared under hydrothermal conditions, yet the average pore diameter is ca. 7 nm for the



commercial sample, while the other three samples at ca. 17 nm. The type of N<sub>2</sub> isotherms for commercial alumina was rather different from the as-prepared alumina samples. The type IV isotherm suggests that the commercial alumina was ascribed to typical mesoporous material, [31] and the type II isotherm for the as-prepared alumina indicate the presence of relatively larger mesopores, which can be ascribed to the piled pore system generated by the stacking particles. The hysteresis loops of the as-prepared alumina samples also shift to a higher N<sub>2</sub> partial pressure compared to the commercial alumina, which is consistent with the much broader pore size distribution [32].

The Ni/Mo oxides were loaded on the alumina samples via the impregnation method followed by calcination in the air. The N<sub>2</sub> adsorption–desorption isotherms and pore diameter distributions almost maintained after the loading of the active component, with a predictable shrinkage in specific surface area and pore volume (Figure S1). As is shown in Figure 2, the corresponding XRD patterns of the as-prepared catalysts also retained diffraction peaks at 19.8°, 31.9°, 37.4°, 39.7°, 46.8°, and 66.9° for  $\gamma$ -Al<sub>2</sub>O<sub>3</sub> phase. However, no XRD peaks corresponding to nickel and molybdenum species were observed for the NiMo/AN and NiMo/CA samples, which could be attributed to the highly dispersed nickel and molybdenum species. For comparison, small peaks arise on NiMo-AR and NiMo-AH catalysts, which indicated the formation of nickel aluminum oxide. And for the sulfide catalysts, broad peaks arising at 14.4, 33.5, 39.5, and 58.6°, which could be attributed to (002), (101), (103), and (110) crystal planes of MoS<sub>2</sub> phase (JCPDS37-1492, Figure S2).

H<sub>2</sub>-temperature-programmed reduction experiments were performed to investigate the interactions between NiMo species and the support as well as their redox properties (Figure 3). All the catalysts exhibit two main reduction peaks located at cal. 710 and 1100 K, representing the partial reduction of Mo<sup>6+</sup>–Mo<sup>4+</sup> of the Mo species, and the second step of reduction of the Mo species, respectively. The shoulder peak at cal. 900 K could be attributed to the reduction of Ni<sup>2+</sup> species on the surface of alumina support [33]. Compared with the NiMo/CA samples, the reduction peaks of NiMo/AN catalyst shift slightly to a lower temperature, indicating the Ni and Mo species were more easily reduced on the AN. Moreover, the peak area for the partial reduction of Mo<sup>6+</sup> for NiMo/CA is smaller than the other three samples, and the shoulder peak is located at a significantly higher temperature region. The above results show that the Ni and Mo species on the nanorod alumina that prepared under hydrothermal conditions were more easily reduced than that on the commercial alumina. However, the NiMo/AH and NiMo/AR with a lower dosage of {111} facet exhibit reduction region at a slightly higher temperature region, indicating relatively increased interaction between metal and the support than the commercial alumina.

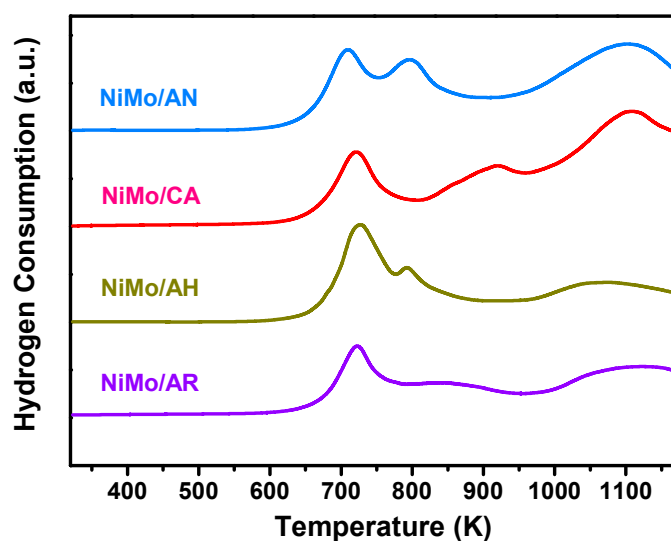


Figure 3. H<sub>2</sub>-temperature-programmed reduction (TPR) profiles of the NiMo/Al<sub>2</sub>O<sub>3</sub> catalysts.

The XPS spectra of the sulfurized catalysts were collected in Figure 4 to characterize the bonding state of the NiMo/Al<sub>2</sub>O<sub>3</sub> samples. For the NiMo series catalysts in the sulfided state, the sulfidation degree of Mo and the formation of the NiMoS phase are considered to be vital in determining their HDS performance. Therefore, the deconvolution results of Mo 3d and Ni 2p spectra are also well documented. According to previous studies, the binding energy of Mo<sup>IV</sup> (3d<sub>5/2</sub>) located at  $228.8 \pm 0.2$  eV can be attributed to the disulfide phase (MoS<sub>2</sub>). For the Mo oxide species (Mo<sup>VI</sup>3d<sub>5/2</sub>), the binding energy is located at  $232.6 \pm 0.2$  eV. An intermediate phase (Mo<sup>V</sup> 3d<sub>5/2</sub>) were found to be located at  $230.6 \pm 0.2$  eV, which can be identified as MoO<sub>x</sub>S<sub>y</sub> species. The peak centered at 226.0 eV is assigned to the S 2s [31,34]. The atomic fraction for the sulfided phases of MoS<sub>2</sub> is 88.3%, 87.2%, 85.0%, and 80.8% for NiMo/AN, NiMo/CA, NiMo/AH, and NiMo/AR catalysts, respectively. Compared with the other three catalysts, the Mo sulfidation and reduction is promoted for NiMo/AN sample, which can be attributed to the relatively weak interaction between Mo species and the alumina support. Moreover, the surface Mo/Al of all the catalysts obtained by XPS is higher than the Mo/Al obtained by XRF (Table 4), suggesting that the Mo species was well dispersed on the surface of Alumina support.

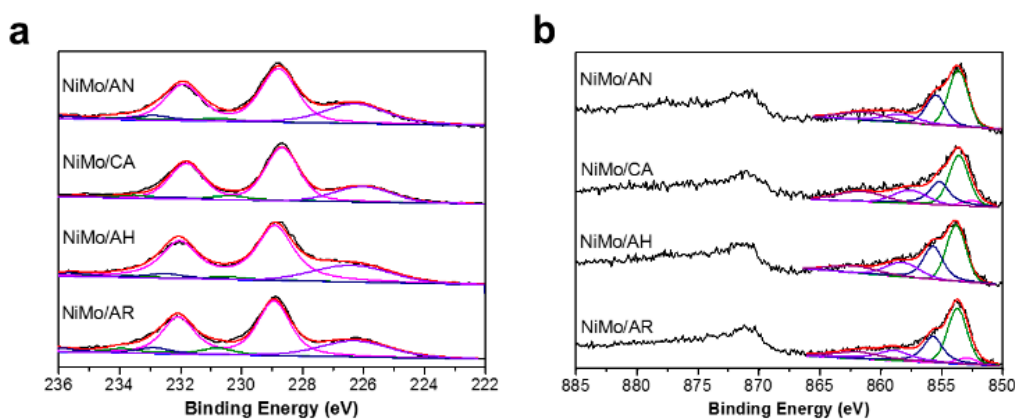


Figure 4. Mo 3d (a) and Ni 2p (b) XPS spectra of the alumina supported NiMoS samples.

Ni 2p spectra are showed in Figure 4b. The binding energy of the NiMoS phase is located at  $853.7 \pm 0.2$  eV, and the binding energy for NiS<sub>x</sub> species is located at  $853.0 \pm 0.1$  eV. The peak at  $856 \pm 0.2$  eV is assigned to NiO species. As a supplement, the remaining two broad peaks are satellite lines of the corresponding Ni species. The fraction of NiMoS phase for NiMo/AN is higher than the other three samples, in accordance with the fitting result of the atomic fraction for the Mo<sup>IV</sup> phase (Tables 2 and 3). For the three supports prepared under different pH, the fraction of the MoS<sub>2</sub> phase decreased with increased pH value, meaning that the sulfidation degree is promoted with increased {111} surface exposure. This can be rationalized that for the alumina surfaces, the capacity of Mo atoms and the sulfidation rate are relatively higher on {111} facet of  $\gamma$ -Al<sub>2</sub>O<sub>3</sub> [10]. In previous research, the {111} facets on  $\gamma$ -Al<sub>2</sub>O<sub>3</sub> was recognized as an analog to the (0001) surface of  $\alpha$ -Al<sub>2</sub>O<sub>3</sub> base on their similar array of Al and O atoms [35]. In our research to study interactions between support and active phases, however, the A (11 $\bar{2}$ 0) and M (10 $\bar{1}$ 0) surfaces of  $\alpha$ -Al<sub>2</sub>O<sub>3</sub> are considered as better models for the (100) and {111} facets of  $\gamma$ -Al<sub>2</sub>O<sub>3</sub> owing to the similarity in surface OH species [9]. The results coordinate well with the {111} facet portion calculated by TEM measurement.

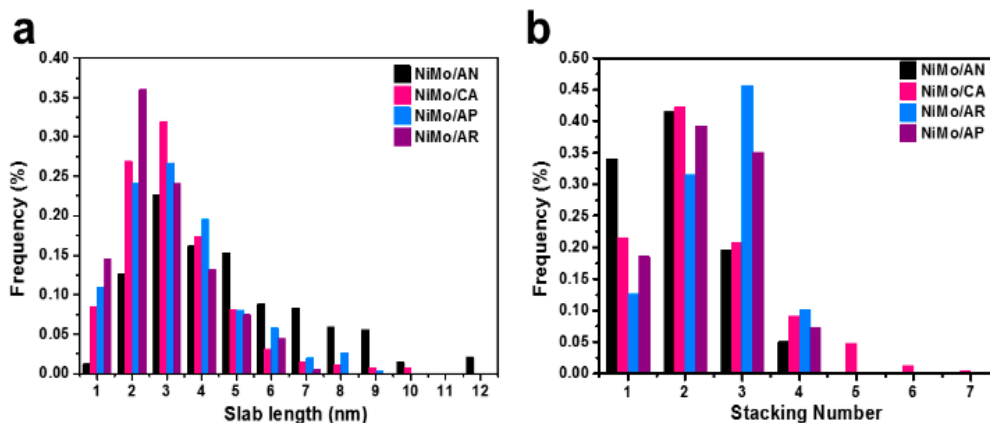
The dispersion of MoS<sub>2</sub> is further determined by HRTEM measurement (Figure 5). The results were summarized in Table 4. The MoS<sub>2</sub> clusters can be observed in all the sulfided catalysts, with 6.2 Å interplanar distance and mostly stacked up 1 to 3 layers. The lengths and stacking numbers of the MoS<sub>2</sub> nano slabs on the sulfided catalysts were quantified. The statistical analyses were based on at least 20 images of 300–400 slabs (Figure 6) from varied parts of each catalyst.

**Table 2.** Fractions of Mo species in the sulfided catalysts by XPS analysis.

Catalysts	Mo(IV)		Mo(V)		Mo(VI)	
	BE(eV)	%/atm.	BE(eV)	%/atm.	BE(eV)	%/atm.
NiMo/AN	228.8	88.3	230.5	4.9	232.4	7.9
NiMo/CA	228.7	87.2	230.5	8.4	232.5	4.4
NiMo/AH	228.8	85.0	230.6	5.9	232.5	9.1
NiMo/AR	228.8	80.8	230.6	10.0	232.5	9.2

**Table 3.** Fractions of Ni species in the sulfide catalysts by XPS analysis.

Catalysts	NiMoS Phase		NiS <sub>x</sub> Phase		NiO <sub>x</sub> Phase	
	BE(eV)	%/atm.	BE(eV)	%/atm.	BE(eV)	%/atm.
NiMo/AN	853.7	61.4	853.0	1.3	855.9	37.3
NiMo/CA	853.7	58.4	853.0	5.9	856.0	35.7
NiMo/AH	853.6	58.0	853.0	7.7	855.9	34.3
NiMo/AR	853.6	57.1	853.0	1.2	856.0	41.7

**Figure 5.** (a) Length and (b) stacking distribution for MoS<sub>2</sub> slabs over sulfided NiMo/Al<sub>2</sub>O<sub>3</sub> catalysts.**Table 4.** Typical properties of the NiMoS catalysts.

Catalysts	$L_s$ (nm) <sup>a</sup>	$N_s$ <sup>b</sup>	$f_{Mo}$ <sup>c</sup>	Mo/Al <sup>d</sup>	Ni/(Ni+Mo) <sup>d</sup>	Mo/Al <sup>e</sup>
NiMo/AN	6.14	1.96	0.13	0.077	0.45	0.046
NiMo/CA	3.75	2.32	0.17	0.073	0.49	0.047
NiMo/AH	3.35	2.31	0.18	0.069	0.49	0.048
NiMo/AR	3.87	2.53	0.17	0.068	0.53	0.046

<sup>a</sup> average slab length of MoS<sub>2</sub> nano slabs; <sup>b</sup> average slab length of MoS<sub>2</sub> nano slabs; <sup>c</sup> calculated dispersion of MoS<sub>2</sub>; <sup>d</sup> molar ratios obtained by XPS; <sup>e</sup> molar ratios obtained by XRF.

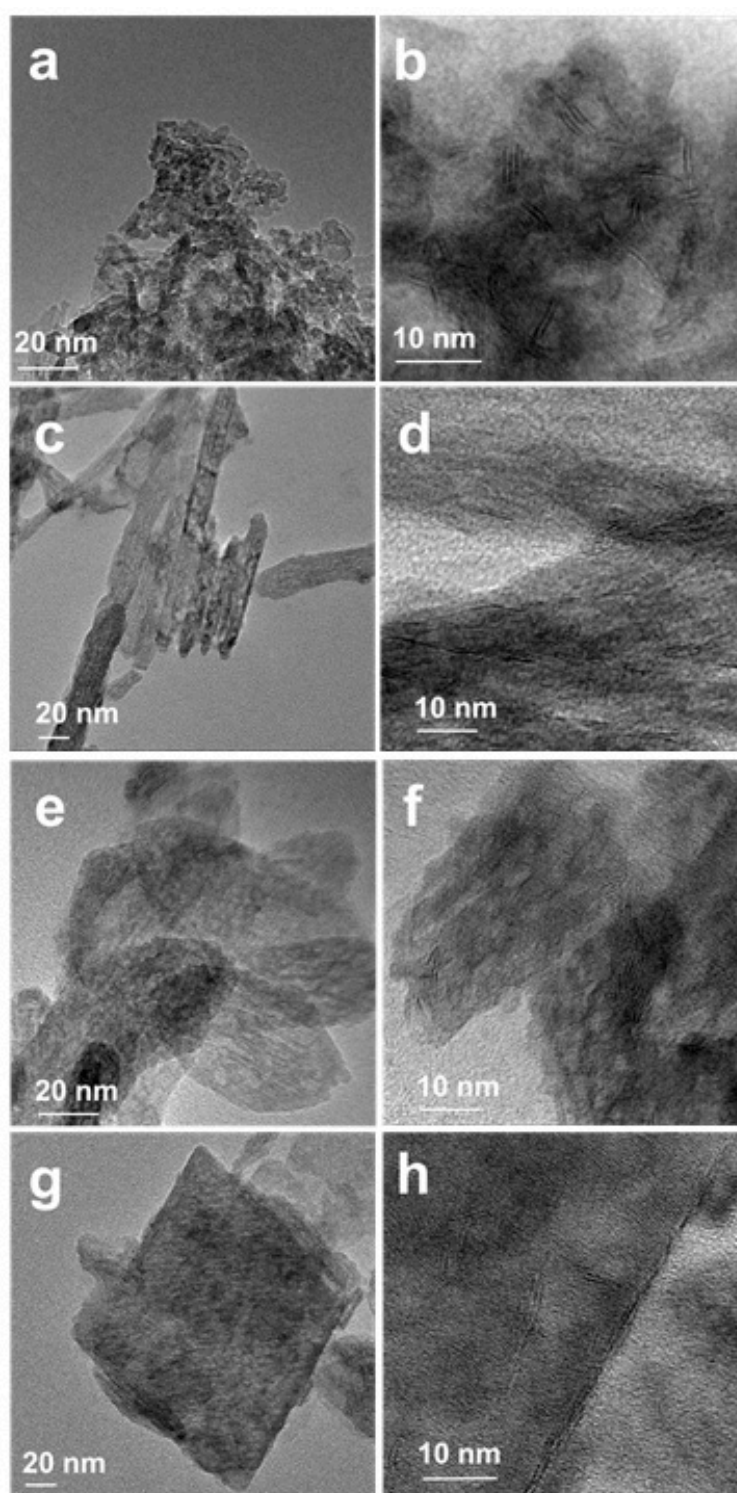


**Figure 6.** Typical HRTEM images of sulfided (a,b) NiMo/CA, (c,d) NiMo/AN, (e,f) NiMo/AH, (g,h) NiMo/AR catalysts.

The average slab length ( $L_s$ ) and stacking number ( $N_s$ ) were calculated based on the following equations.

$$L_s = \sum_{i=1}^x x_i l_i / \sum_{i=1}^x x_i, \quad (1)$$



$$N_s = \sum_{i=1}^y y_i n_i N_i / \sum_{i=1}^y y_i, \quad (2)$$

where  $l_i$  stands for the length of slab  $i$ ,  $N_i$  is the layer number of slab  $i$ ,  $x_i$  stands for the slab number with a length of  $l_i$ , and  $y_i$  stands for the number of slabs with stacking numbers of  $n_i$ . The results of length and stacking conditions for the MoS<sub>2</sub> crystallites over the sulfided catalysts are summarized in Table 4. Usually, the average fraction of Mo atoms located on the edge of the crystallites (donated as  $f_{Mo}$ ) is determined to indicate the dispersion of reactive surface on the active phase. Assuming the MoS<sub>2</sub> slabs were perfect hexagons, the value of  $f_{Mo}$  is defined with the following Equation (3) [36]

$$f_{Mo} = \sum_{i=1}^t (6n_i - 6) / \sum_{i=1}^t (3n_i^2 - 3n_i + 1), \quad (3)$$

where the  $n_i$  (determined by the length of MoS<sub>2</sub> slabs,  $L = 3.2(2n_i - 1) \text{ \AA}$ ) represents the number of Mo atoms located along one edge of a single MoS<sub>2</sub> nano slab, and  $t$  represents the total number of MoS<sub>2</sub> slabs observed from TEM images. The results in Table 4 show that no significant difference was observed in the average slab length ( $L_s$ ) and stacking number ( $N_s$ ) of MoS<sub>2</sub> over the NiMo/CA, NiMo/AH, and NiMo/AR catalysts ( $L_s = \text{ca. } 3\sim 4 \text{ nm}$ ,  $N_s = \text{ca. } 2.3\sim 2.6$ ). Especially, the  $L_s$  for NiMo/AN catalyst shows a significantly larger value (6.14 nm), while its'  $N_s$  value is relatively low (1.96). Therefore, the NiMo/AN sample presents the lowest calculated dispersion among the relevant catalysts.

By observing on TEM images together with the calculated parameters, it can be concluded that the MoS<sub>2</sub> crystallites formed on CA, AH, and AR are similar in length as well as stacking numbers. In contrast, the average length of MoS<sub>2</sub> on AN is much longer than the other catalysts. Most of the MoS<sub>2</sub> nano slabs are located along the long side of the rods, or intersections of the rods. The MoS<sub>2</sub> nanocrystallites grown along the rods tend to form long nano slabs with low stacking numbers (mostly 1 stack, Figure 6d), indicating a relatively weak interaction between the active phase and the support, which result in longer crystal length and high sulfidation degree. This result is different from previous reports about MoS<sub>2</sub> over commercial alumina.

### 2.3. HDS Performance of Thiophene and Dibenzothiophene over NiMo/Al<sub>2</sub>O<sub>3</sub> Catalysts

The catalytic behavior is determined by the structural and chemical features of the catalysts. A thiophene HDS test over the sulfided NiMo/Al<sub>2</sub>O<sub>3</sub> catalysts was carried out at 523 K under atmospheric conditions. The proposed reaction network (Scheme S2) shows that HDS of thiophene occurs through two parallel pathways involving direct desulfurization (DDS) to butadiene and n-butene and sequential hydrogenation (HYD) to dihydrothiophene and then tetrahydrothiophene followed by sulfur removal, and finally, n-butane was formed. The as mentioned four NiMo catalysts show stable conversion at 60–80% throughout the whole evaluation process, and the thiophene conversion increased in the following order: NiMo/AN > NiMo/CA > NiMo/AH > NiMo/AR (Figure 7). Interestingly, despite presenting the largest surface area (254.8 m<sup>2</sup>/g) and pore volume (0.68 cm<sup>3</sup>/g), which were considered of great importance in previous research, the NiMo/CA sample was less effective than the NiMo/AN sample in the conversion of thiophene, which can be rationalized by the higher exposure of high-energy external {111} surface on NiMo/AN. As discussed in previous sections, the AN sample with higher exposure of {111} facets, which can accommodate more Mo atoms with higher sulfidation degree.

In order to evaluate the {111} facet exposure of  $\gamma$ -alumina support on the HDS activity, a factor of  $S_{(111)}$  was defined to minimize the effect of the difference in surface area. Also, the turnover frequency (TOF) was calculated by using the  $f_{Mo}$  acquired by HRTEM analysis and the concentration of MoS<sub>2</sub> phase by XPS analysis. It can be seen from Figure 8 that the calculation of turnover frequencies for HDS of thiophene increased exponentially with the increasing value of  $S_{(111)}$ , where  $S_{(111)} = S_{BET} \cdot p$  has been calculated and  $p$  represents the proportion of {111} facet (Table 1). The result shows the

great contribution of {111} facet on the activity of HDS reactions of thiophene, which can be tuned by controlling the morphology of the alumina support.

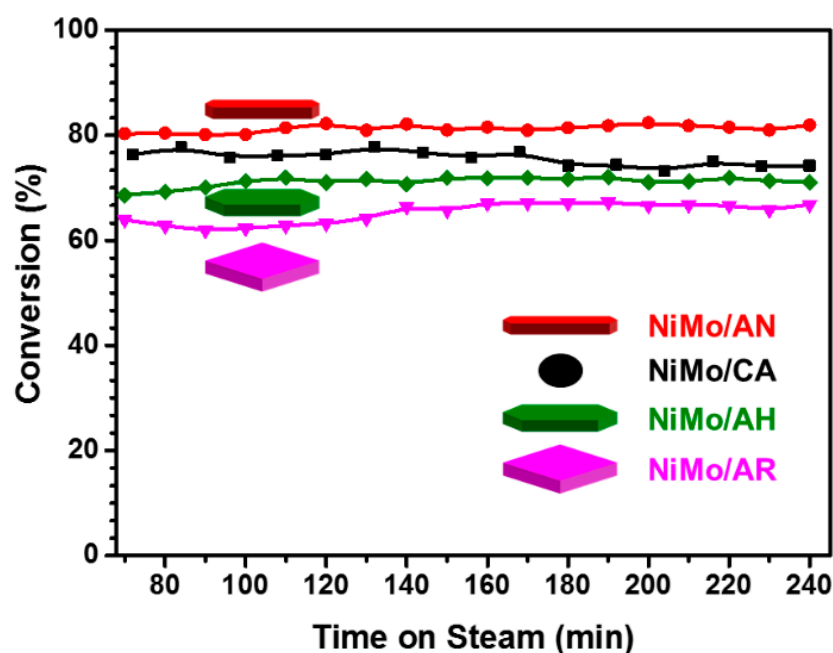


**Figure 7.** Hydrodesulfurization (HDS) of thiophene under atmospheric pressure at 525 K (red: NiMo/AN, black: NiMo/CA, green: NiMo/AH, pink: NiMo/AR).

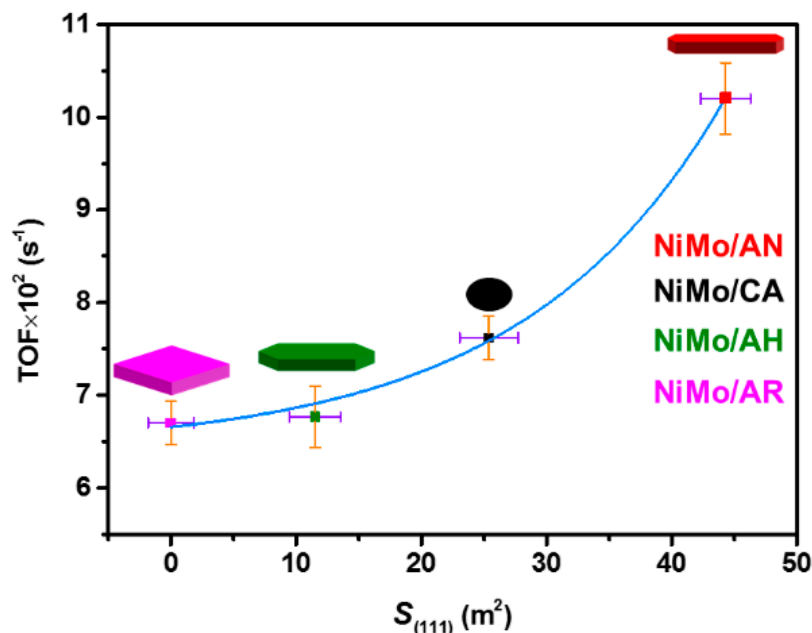


**Figure 8.** Average turnover frequency (TOF,  $s^{-1}$ ) of thiophene HDS activity over sulfided NiMo/ $Al_2O_3$  catalysts as a function of an increased portion of {111} facets.

Finally, the bulkier sulfur-containing compound dibenzothiophene (DBT, which also occurs through two parallel routes), was also selected as a model compound to evaluate the HDS activity of these catalysts. The HDS reaction of DBT was tested under 533 K with an  $H_2$ /oil ratio of 600/1 ( $v/v$ ), a liquid hour space velocity (LHSV) of  $4 h^{-1}$ , and a total pressure of 1.5 MPa. The results revealed that HDS activities towards DBT over different catalysts were ranked in the order of

NiMo/AN > NiMo/CA > NiMo/AH > NiMo/AR, which is in accordance with their thiophene HDS activity. The product distribution and HYD/DDS ratio for the sulfided catalysts were further compared in Table S1. The selectivity of biphenyl (BP) (which is generated via the DDS pathway) reached over 85% for all the catalysts, much higher than the products formed through the HYD route. All the catalysts show a similar HYD/DDS ratio. The results demonstrate that the NiMo/AN catalyst exhibit the best HDS catalytic performance towards DBT and thiophene, and also the crucial of {111} facet on the HDS catalytic reaction over  $\gamma$ -Al<sub>2</sub>O<sub>3</sub>. The correlation of {111} facet ratio and HDS reaction activity over  $\gamma$ -Al<sub>2</sub>O<sub>3</sub> provide direct evidence for the positive role of {111} facet on HDS reaction.

### 3. Experimental Sections

#### 3.1. Materials

All of the materials used were purchased from Sinopharm Chemical Reagent Co. (Shanghai, China) and were used without further purification, except that the dibenzothiophene (DBT) was purchased from Sigma-Aldrich (St. Louis, MO, USA). In addition, the commercial alumina support (denoted as CA) used as a control was obtained from the Fushun Research Institute of Petroleum and Petrochemical, SINOPEC (Fushun, China).

#### 3.2. Preparation of $\gamma$ -Alumina Support

A series of Al<sub>2</sub>O<sub>3</sub> nanoparticles were prepared based on previous reports with slight modification [37]. A typical preparation process was as follows. 9.66 g of AlCl<sub>3</sub>·6H<sub>2</sub>O was dissolved into 20 mL of distilled water. 60 mL of an aqueous solution of ammonia (1 M) was added into the solution dropwise under drastic stirring until the pH = 5. Then the obtained slurry was aged at room temperature for 2 h. The resultant was centrifuged at 10,000 rpm and the remaining gel was adjusted to targeted pH (depicted in Table 1) by ammonia or acetic acid solution. The gels were then sealed in a Teflon-lined stainless steel autoclave heated at 473 K for 24 h. After the autoclave was cooled down to room temperature, the samples were collected and washed with distilled water. After being dried at 393 K overnight, the samples were calcined in a muffle furnace at 823 K for 4 h at a heating rate of 2 K per minute.

#### 3.3. Preparation of HDS Catalysts

The HDS catalysts were prepared by loading the precursors of active components (Ni and Mo salts) on the alumina via the simultaneous incipient wetness impregnation method. The precursors ((NH<sub>4</sub>)<sub>6</sub>Mo<sub>7</sub>O<sub>24</sub>·24H<sub>2</sub>O and Ni(NO<sub>3</sub>)<sub>2</sub>·6H<sub>2</sub>O) were mixed and well dispersed in deionized water. After impregnation, the catalysts were then dried at 393 K overnight and calcined in flowing air at 773 K for 3 h. The final loading amount is 3.0 wt. % of NiO and 12.0 wt. % of MoO<sub>3</sub> for each catalyst.

#### 3.4. Characterization

The N<sub>2</sub> adsorption–desorption measurements of the composite were performed on a Micromeritics Tristar 3020 adsorption automatic instrument. Before the measurement, the samples were pretreated at 573 K for 3 h in vacuum to remove the adsorbed impurities. The specific surface area and pore volume of the catalysts were calculated from nitrogen adsorption–desorption isotherms using the Brunauer–Emmett–Teller (BET) and Barrett–Joyner–Halenda (BJH) methods. Powder X-ray diffraction (XRD) characterization was carried out over a RigakuUltima IV automatic powder diffractometer (Rigaku Co., Ltd., Tokyo, Japan) operated at 40 kV and 30 mA using Cu K $\alpha$  ( $\lambda$  = 0.15406 nm) monochromatized radiation with a scan speed of 10° per minute. After acquiring the profiles, the JCPDS file database was used for peak identification. Regular transmission electron microscopy (TEM) images were obtained by a JEM-1400 (JEOL Ltd, Tokyo, Japan) at 100 kV, and high-resolution transmission electron microscopy (HRTEM) images of the samples were obtained using a Jeol JEM-2100F Field Emission Electron Microscope (JEOL Ltd, Tokyo, Japan) operating at 200 kV. The composites to

be measured were ultrasonically dispersed in ethanol, and the dispersed suspensions were dropped onto carbon-coated copper grids before TEM observation.

Temperature-programmed reduction (TPR) of the catalysts in oxidation state was performed on a GC-TPR apparatus. Then, 50 mg of the catalyst was pre-purged with an argon stream at  $30 \text{ mL min}^{-1}$  at 573 K for 1 h and then cooled to 325 K. The sample was then heated to 1173 K at a rate of  $10 \text{ K min}^{-1}$  under a 5%  $\text{H}_2/\text{Ar}$  flow ( $50 \text{ mL min}^{-1}$ ).

X-ray Fluorescence (XRF) analyses were performed on an Amptek X-123 X-ray spectrometer (Amptek, Inc., Bedford, MA, USA) with Si-PIN photodiode. The X-ray spectrometer contains a solid-state detector, a digital pulse processor, and a multichannel analyzer, which are interfaced with a computer for data acquisition and analysis. A  $25 \text{ }\mu\text{m}$  thick silver filter and a  $250 \text{ }\mu\text{m}$  thick aluminum filter were simultaneously used to reduce background and improve the signal-to-noise ratio (SNR) in the energy region (10–30 keV) of the XRF spectrum.

The X-ray photoelectron spectroscopy (XPS) measurements were performed with a MultiLab 2000 spectrometer (Thermo Electron Co. (Thermo Nicolet), Madison, USA) using  $\text{Mg K}\alpha$  radiation under vacuum ( $<10^{-9}$  mbar). The as-prepared sulfurized samples were kept in a nitrogen atmosphere to prevent oxidation prior to XPS analysis. The C 1s peak at 284.6 eV was used as an internal standard to compensate for sample charging. To quantify the Ni and Mo species contents, the XPS spectra were fitted using XPSPEAK software (XPSPEAK 4.1). The background was subtracted according to Shirley and quantification was performed using the sensitivity factors reported by Wagner et al. [38] The Mo3d and Ni2p spectra were deconvoluted by fitting the experimental spectra to a mixed Gaussian–Lorentzian function in which the Lorentzian function takes a fraction of 70–80%. Moreover, the XPS uncertainties are about 5%.

### 3.5. Catalytic Performance Evaluation

Thiophene HDS activity of NiMoS catalysts was measured in a fixed-bed flow microreactor at atmospheric pressure with a thiophene/ $\text{H}_2$  molar ratio of 1/10 and a ratio of thiophene molar flow to catalyst mass  $2.8 \times 10^{-5} \text{ mol g}^{-1} \text{ s}^{-1}$ . For each run, 200 mg of the catalyst with 40–60 mesh of particle size was diluted with quartz pellets to a constant volume of 0.5 mL before being placed in the quartz reactor. The sample was presulfurized in situ at 673 K for 2 h under a 15 vol%  $\text{H}_2\text{S}/\text{H}_2$  flow and then was reduced to the targeted temperature at 525 K. The products were analyzed using an on-line gas chromatograph equipped with an FID detector. The thiophene conversion was calculated by measuring the mole ratio between butane in the product and total thiophene in the feedstock.

The dibenzothiophene (DBT) hydrodesulfurization activity of the catalysts was evaluated in a high-pressure fixed-bed continuous-flow stainless steel reactor, using 2.0 wt. % DBT in cyclohexane as a model compound. For each run, 100 mg of the catalyst (20–40 mesh particle size), which was diluted with 400 mg quartz pellets, was presulfided at 673 K at a flow rate of  $40 \text{ mL min}^{-1}$  of 15%  $\text{H}_2\text{S}/\text{H}_2$  under atmospheric pressure. The tests were stabilized at 533 K with a total pressure of 1.5 MPa, a liquid hour space velocity (LHSV) of  $4 \text{ h}^{-1}$ , and an  $\text{H}_2/\text{oil}$  ratio of 600/1 ( $v/v$ ). The liquid products were collected and analyzed by a gas chromatograph (GC-9560) equipped with an FID detector and SE-30 capillary column. The reaction products were identified by matching their retention times with those of the commercial standards together with GC/MS analysis using a Finnigan Trace DSQ. The rate of thiophene transformation was calculated as  $R = (F/m)X$ , where  $R$  is the specific rate expressed as moles of thiophene transformed per second and per gram of catalyst,  $F$  is the molar flow rate of thiophene,  $m$  represents the mass of the catalyst, and  $X$  is the fractional conversion of thiophene. TOF (turnover frequency) is defined as the number of reacted thiophene molecules per second and per Mo atom at the edge surface [36], which can be determined by  $f_{\text{Mo}}$  and the surface concentration of the  $\text{MoS}_2$  phase (obtained from XPS results).

### 3.6. Calculation of the Facet Ratio by TEM Measurements

The length and thickness of alumina nanoparticles were measured on TEM images of 50 particles for each pH condition. Usually, the main facets are discussed based on (100), (110), and (111) facets [39]. The calculation of the facet ratio was done based on the measured parameters which are described in Scheme S1.

### 3.7. Calculation of the Slab Length ( $L_{\text{MoS}_2}$ ) and Stacking Numbers ( $N_{\text{MoS}_2}$ ) of $\text{MoS}_2$ Nanoslabes by TEM Measurements

The dispersion of  $\text{MoS}_2$  nano slabs in sulfided catalysts was measured by HRTEM observation. For each sample, ca. 300  $\text{MoS}_2$  nano slabs in about 30 HRTEM images were obtained to calculate slab length ( $L_M$ ) and stacking numbers ( $S_N$ ) [40].

## 4. Conclusions

In this work, in exploring adequate alumina support for highly active HDS catalysts, a sample with varied exposure of high-energy {111} facet is successfully prepared via hydrothermal synthesis. The alumina nanorods support with the highest dose of {111} constituent, though low in total surface area, is more active than other counterparts in HDS reactions of thiophene and dibenzothiophene. These intriguing results also demonstrate the adequate control of morphology and exposed facets have an important influence over the HDS activities of  $\text{NiMo}/\text{Al}_2\text{O}_3$  catalyst and provide guidance in the rational design of hydrotreating catalyst support on the facet scale.

**Supplementary Materials:** The following are available online at <http://www.mdpi.com/2073-4344/10/11/1254/s1>, Scheme S1: Schematic description of  $\gamma\text{-Al}_2\text{O}_3$  with the indexing of the dimensional parameters, Scheme S2: Proposed reaction network of thiophene over HDS catalysts through DDS (direct desulfurization) and HYD (hydrodesulfurization) pathways, Figure S1:  $\text{N}_2$  adsorption-desorption isotherms and pore size distribution curves for (a)  $\gamma$ -alumina and (b)  $\text{NiMo}/\gamma$ -alumina catalysts, Figure S2: XRD of the  $\text{NiMoS}/\text{Al}_2\text{O}_3$  samples, Table S1: HDS of DBT under 1.6 MPa at 525 K, Table S2: Texture properties of as prepared alumina after loading with Ni and Mo.

**Author Contributions:** Y.X., S.L., X.Y., and W.F. conceived the research grants and discussed the study. Y.X., L.S., X.H., Y.Z., and W.L. fabricated the samples, performed XRD, SEM, XPS, TEM, and BET experiments. Y.X. measured the catalytic performance. Y.X., S.L., X.Y., and W.F. discussed the manuscript. Y.X. and X.Y. wrote the manuscript. All authors discussed the results and commented on the manuscript. All authors have read and agreed to the published version of the manuscript.

**Funding:** This research received no external funding.

**Acknowledgments:** This work is supported by the National Natural Science Foundation of China (22072057, 21773194 and 21703179), and the Fundamental Research Funds for the Central Universities of China (20720170103).

**Conflicts of Interest:** The authors declare no conflict of interest.

## References

- dos Santos, A.S.; Girard, E.; Leflaive, P.; Brunet, S. Competitive adsorptions between thiophenic compounds over a  $\text{CoMoS}/\text{Al}_2\text{O}_3$  catalyst under deep HDS of FCC gasoline. *Appl. Catal. A: Gen.* **2019**, *570*, 292–298. [CrossRef]
- Zhang, H.; Lin, H.; Zheng, Y. Application of Uniform Design Method in the Optimization of Hydrothermal Synthesis for Nano  $\text{MoS}_2$  Catalyst with High HDS Activity. *Catalysts* **2018**, *8*, 654. [CrossRef]
- Neto, A.V.d.; Leite, E.R.; da Silva, V.T.; Zotin, J.L.; Urquieta-González, E.A.  $\text{NiMoS}$  HDS catalysts – The effect of the Ti and Zr incorporation into the silica support and of the catalyst preparation methodology on the orientation and activity of the formed  $\text{MoS}_2$  slabs. *Appl. Catal. A Gen.* **2016**, *528*, 74–85. [CrossRef]
- Okamoto, Y.; Breyse, M.; Dhar, G.M.; Song, C. Effect of support in hydrotreating catalysis for ultra clean fuels. *Catal. Today* **2003**, *86*, 1–3. [CrossRef]
- Puello-Polo, E.; Pájaro, Y.; Márquez, E. Effect of the Gallium and Vanadium on the Dibenzothiophene Hydrodesulfurization and Naphthalene Hydrogenation Activities Using Sulfided  $\text{NiMo-V}_2\text{O}_5/\text{Al}_2\text{O}_3\text{-Ga}_2\text{O}_3$ . *Catalysts* **2020**, *10*, 894. [CrossRef]



6. Li, F.; Liang, J.; Zhu, W.; Song, H.; Wang, K.; Li, C. High Active Zn/Mg-Modified Ni-P/Al<sub>2</sub>O<sub>3</sub> Catalysts Derived from ZnMgNiAl Layered Double Hydroxides for Hydrodesulfurization of Dibenzothiophene. *Catalysts* **2017**, *7*, 202. [\[CrossRef\]](#)
7. Abdelkader, A.; Osman, A.I.; Halawy, S.A.; Mohamed, M.A. Preparation and characterization of mesoporous  $\gamma$ -Al<sub>2</sub>O<sub>3</sub> recovered from aluminum cans waste and its use in the dehydration of methanol to dimethyl ether. *J. Mater. Cycles Waste Manage.* **2018**, *20*, 1428–1436. [\[CrossRef\]](#)
8. Osman, A.I.; Abu-Dahrieh, J.K.; McLaren, M.; Laffir, F.; Rooney, D.W. Characterisation of Robust Combustion Catalyst from Aluminium Foil Waste. *ChemistrySelect* **2018**, *3*, 1545–1550. [\[CrossRef\]](#)
9. Bara, C.; Devers, E.; Digne, M.; Lamic-Humblot, A.-F.; Pirngruber, G.D.; Carrier, X. Surface Science Approaches for the Preparation of Alumina-Supported Hydrotreating Catalysts. *ChemCatChem* **2015**, *7*, 3422–3440. [\[CrossRef\]](#)
10. Bara, C.; Plais, L.; Larmier, K.; Devers, E.; Digne, M.; Lamic-Humblot, A.F.; Pirngruber, G.D.; Carrier, X. Aqueous-Phase Preparation of Model HDS Catalysts on Planar Alumina Substrates: Support Effect on Mo Adsorption and Sulfidation. *J. Am. Chem. Soc.* **2015**, *137*, 15915–15928. [\[CrossRef\]](#)
11. Arrouvel, C.; Breyse, M.; Toulhoat, H.; Raybaud, P. Effects of P<sub>H2O</sub>, P<sub>H2S</sub>, P<sub>H2</sub> on the surface properties of anatase-TiO<sub>2</sub> and  $\gamma$ -Al<sub>2</sub>O<sub>3</sub>: A DFT study. *J. Catal.* **2005**, *232*, 161–178. [\[CrossRef\]](#)
12. Costa, D.; Arrouvel, C.; Breyse, M.; Toulhoat, H.; Raybaud, P. Edge wetting effects of  $\gamma$ -Al<sub>2</sub>O<sub>3</sub> and anatase-TiO<sub>2</sub> supports by MoS<sub>2</sub> and CoMoS active phases: A DFT study. *J. Catal.* **2007**, *246*, 325–343. [\[CrossRef\]](#)
13. Sakashita, Y.; Araki, Y.; Honna, K.; Shimada, H. Orientation and morphology of molybdenum sulfide catalysts supported on titania particles, observed by using high-resolution electron microscopy. *Appl. J. Catal. A Gen.* **2000**, *197*, 247–253. [\[CrossRef\]](#)
14. Kibsgaard, J.; Clausen, B.S.; Topsøe, H.; Lægsgaard, E.; Lauritsen, J.V.; Besenbacher, F. Scanning tunneling microscopy studies of TiO<sub>2</sub>-supported hydrotreating catalysts: Anisotropic particle shapes by edge-specific MoS<sub>2</sub>-support bonding. *J. Catal.* **2009**, *263*, 98–103. [\[CrossRef\]](#)
15. Liu, Y.; Wang, H.; Liu, Y.; Zhao, J.; Liu, C. Reactive Adsorption Desulfurization on Cu/ZnO Adsorbent: Effect of ZnO Polarity Ratio on Selective Hydrogenation. *Energ. Fuel* **2017**, *31*, 9930–9938. [\[CrossRef\]](#)
16. Sitamraju, S.; Xiao, J.; Janik, M.J.; Song, C. Active Sites on Ti-Ce Mixed Metal Oxides for Reactive Adsorption of Thiophene and Its Derivatives: A DFT Study. *J. Phys. Chem. C* **2015**, *119*, 5903–5913. [\[CrossRef\]](#)
17. Wang, X.; Ding, L.; Zhao, Z.; Xu, W.; Meng, B.; Qiu, J. Novel hydrodesulfurization nano-catalysts derived from Co<sub>3</sub>O<sub>4</sub> nanocrystals with different shapes. *Catal. Today* **2011**, *175*, 509–514. [\[CrossRef\]](#)
18. Laurenti, D.; Phung-Ngoc, B.; Roukoss, C.; Devers, E.; Marchand, K.; Massin, L.; Lemaitre, L.; Legens, C.; Quoineaud, A.-A.; Vrinat, M. Intrinsic potential of alumina-supported CoMo catalysts in HDS: Comparison between  $\gamma$ c,  $\gamma$ T, and  $\delta$ -alumina. *J. Catal.* **2013**, *297*, 165–175. [\[CrossRef\]](#)
19. Stockmann, R.M.; Zandbergen, H.W.; van Langeveld, A.D.; Moulijn, J.A. Investigation of MoS<sub>2</sub> on  $\gamma$ -Al<sub>2</sub>O<sub>3</sub> by HREM with atomic resolution. *J. Mol. Catal. A Chem.* **1995**, *102*, 147–161. [\[CrossRef\]](#)
20. Digne, M.; Sautet, P.; Raybaud, P.; Euzen, P.; Toulhoat, H. Use of DFT to achieve a rational understanding of acid-basic properties of  $\gamma$ -alumina surfaces. *J. Catal.* **2004**, *226*, 54–68. [\[CrossRef\]](#)
21. Wang, Y.; Yang, J.; Gu, R.; Peng, L.; Guo, X.; Xue, N.; Zhu, Y.; Ding, W. Crystal-Facet Effect of  $\gamma$ -Al<sub>2</sub>O<sub>3</sub> on Supporting CrO<sub>x</sub> for Catalytic Semihydrogenation of Acetylene. *ACS Catal.* **2018**, *8*, 6419–6425. [\[CrossRef\]](#)
22. Hayden, T.F.; Dumesic, J.A. Studies of the structure of molybdenum oxide and sulfide supported on thin films of alumina. *J. Catal.* **1987**, *103*, 366–384. [\[CrossRef\]](#)
23. Sakashita, Y. Effects of surface orientation and crystallinity of alumina supports on the microstructures of molybdenum oxides and sulfides. *Surf. Sci.* **2001**, *489*, 45–48. [\[CrossRef\]](#)
24. Sakashita, Y.; Yoneda, T. Orientation of MoS<sub>2</sub> Clusters Supported on Two Kinds of  $\gamma$ -Al<sub>2</sub>O<sub>3</sub> Single Crystal Surfaces with Different Indices. *J. Catal.* **1999**, *185*, 487–495. [\[CrossRef\]](#)
25. Bara, C.; Lamic-Humblot, A.-F.; Fonda, E.; Gay, A.-S.; Taleb, A.-L.; Devers, E.; Digne, M.; Pirngruber, G.D.; Carrier, X. Surface-dependent sulfidation and orientation of MoS<sub>2</sub> slabs on alumina-supported model HDS catalysts. *J. Catal.* **2016**, *344*, 591–605. [\[CrossRef\]](#)
26. Wang, L.; Liu, H.; Fan, Y.; Yuan, P.; Huang, D.; Oyama, S.T.; Wang, T.; Bao, X. Cooperative bimetallic catalyst for thio-etherification reaction prepared by crystal-facet engineering of  $\gamma$ -Al<sub>2</sub>O<sub>3</sub> support. *Catal. Today* **2020**. [\[CrossRef\]](#)
27. Krokidis, X.; Raybaud, P.; Gobichon, A.-E.; Rebours, B.; Euzen, P.; Toulhoat, H. Theoretical Study of the Dehydration Process of Boehmite to  $\gamma$ -Alumina. *J. Phys. Chem. B* **2001**, *105*, 5121–5130. [\[CrossRef\]](#)

28. Cai, W.; Zhang, S.; Lv, J.; Chen, J.; Yang, J.; Wang, Y.; Guo, X.; Peng, L.; Ding, W.; Chen, Y.; et al. Nanotubular Gamma Alumina with High-Energy External Surfaces: Synthesis and High Performance for Catalysis. *ACS Catal.* **2017**, *7*, 4083–4092. [\[CrossRef\]](#)
29. Lee, J.; Jang, E.J.; Jeong, H.Y.; Kwak, J.H. Critical role of (100) facets on  $\gamma$ -Al<sub>2</sub>O<sub>3</sub> for ethanol dehydration: Combined efforts of morphology-controlled synthesis and TEM study. *Appl. Catal. A Gen.* **2018**, *556*, 121–128. [\[CrossRef\]](#)
30. Kovarik, L.; Genc, A.; Wang, C.; Qiu, A.; Peden, C.H.F.; Szanyi, J.; Kwak, J.H. Tomography and High-Resolution Electron Microscopy Study of Surfaces and Porosity in a Plate-like  $\gamma$ -Al<sub>2</sub>O<sub>3</sub>. *J. Phys. Chem. C* **2013**, *117*, 179–186. [\[CrossRef\]](#)
31. Dong, Y.; Xu, Y.; Zhang, Y.; Lian, X.; Yi, X.; Zhou, Y.; Fang, W. Synthesis of hierarchically structured alumina support with adjustable nanocrystalline aggregation towards efficient hydrodesulfurization. *Appl. Catal. A Gen.* **2018**, *559*, 30–39. [\[CrossRef\]](#)
32. Lai, W.; Song, W.; Pang, L.; Wu, Z.; Zheng, N.; Li, J.; Zheng, J.; Yi, X.; Fang, W. The effect of starch addition on combustion synthesis of NiMo–Al<sub>2</sub>O<sub>3</sub> catalysts for hydrodesulfurization. *J. Catal.* **2013**, *303*, 80–91. [\[CrossRef\]](#)
33. Ali, S.A.; Ahmed, S.; Ahmed, K.W.; Al-Saleh, M.A. Simultaneous hydrodesulfurization of dibenzothiophene and substituted dibenzothiophenes over phosphorus modified CoMo/Al<sub>2</sub>O<sub>3</sub> catalysts. *Fuel Process. Technol.* **2012**, *98*, 39–44. [\[CrossRef\]](#)
34. Lai, W.; Xu, Y.; Ren, Y.; Yang, L.; Zheng, J.; Yi, X.; Fang, W. Insight into the effect of non-stoichiometric sulfur on a NiMoS hydrodesulfurization catalyst. *Catal. Sci. Technol.* **2016**, *6*, 497–506.
35. Zhang, Z.; Pinnavaia, T.J. Mesoporous  $\gamma$ -Al<sub>2</sub>O<sub>3</sub> with a lathlike framework morphology. *J. Am. Chem. Soc.* **2002**, *124*, 12294–12301. [\[CrossRef\]](#)
36. Fan, Y.; Xiao, H.; Shi, G.; Liu, H.; Qian, Y.; Wang, T.; Gong, G.; Bao, X. Citric acid-assisted hydrothermal method for preparing NiW/USY–Al<sub>2</sub>O<sub>3</sub> ultradeep hydrodesulfurization. *J. Catal.* **2011**, *279*, 27–35. [\[CrossRef\]](#)
37. Zhang, X.; Cui, W.W.; Page, K.L.; Pearce, C.I.; Bowden, M.E.; Graham, T.R.; Shen, Z.Z.; Li, P.; Wang, Z.M.; Kerisit, S.; et al. Size and Morphology Controlled Synthesis of Boehmite Nanoplates and Crystal Growth Mechanisms. *Cryst. Growth Des.* **2018**, *18*, 3596–3606. [\[CrossRef\]](#)
38. Wang, X.; Chaka, A.; Scheffler, M. Effect of the Environment on  $\alpha$ -Al<sub>2</sub>O<sub>3</sub> (0001) Surface Structures. *Phys. Rev. Lett.* **2000**, *84*, 3650–3653. [\[CrossRef\]](#)
39. Lai, W.; Pang, L.; Zheng, J.; Li, J.; Wu, Z.; Yi, X.; Fang, W.; Jia, L. The effect of starch addition on combustion synthesis of NiMo–Al<sub>2</sub>O<sub>3</sub> catalysts for hydrodesulfurization. *Fuel Process. Technol.* **2013**, *110*, 8–16. [\[CrossRef\]](#)
40. Mozhaev, A.V.; Nikulshin, P.A.; Pimerzin, A.A.; Maslakov, K.I.; Pimerzin, A.A. Investigation of co-promotion effect in NiCoMoS/Al<sub>2</sub>O<sub>3</sub> catalysts based on Co<sub>2</sub>Mo<sub>10</sub>-heteropolyacid and nickel citrate. *Catal. Today* **2016**, *271*, 80–90. [\[CrossRef\]](#)

**Publisher’s Note:** MDPI stays neutral with regard to jurisdictional claims in published maps and institutional affiliations.



© 2020 by the authors. Licensee MDPI, Basel, Switzerland. This article is an open access article distributed under the terms and conditions of the Creative Commons Attribution (CC BY) license (<http://creativecommons.org/licenses/by/4.0/>).